Research in Astronomy and Astrophysics, 23:095018 (13pp), 2023 September https://doi.org/10.1088/1674-4527/ace519

Breaking of Large-Scale Filament due to Magnetic Reconnection and Consequent Partial Eruption

Kaifeng Kang[1,2,3,4], Yang Guo[5], Yan Li[1,3,4], Jingxing Wang[1,3,4], and Jun Lin[1,2,3,4]
[1] Yunnan Observatories, Chinese Academy of Sciences, Kunming 650216, China; kkf@ynao.ac.cn, jlin@ynao.ac.cn
[2] University of Chinese Academy of Sciences, Beijing 100049, China
[3] Center for Astronomical Mega-Science, Chinese Academy of Sciences, Beijing 100101, China
[4] Yunnan Key Laboratory of Solar Physics and Space Science, Kunming 650216, China
[5] School of Astronomy and Space Science and Key Laboratory for Modern Astronomy and Astrophysics, Nanjing University, Nanjing 210023, China
Received 2023 May 21; revised 2023 June 3; accepted 2023 June 6; published 2023 August 8

Abstract

Following our previous work, we studied the partial eruption of a large-scale horse-shoe-like filament that had been observed in a decaying active region on the solar disk for more than 4.5 days. The filament became active after it was broken into two pieces, P1 and P2 seen in Hα, by magnetic reconnection between the magnetic field around it and that of a newly emerging active region nearby. P1 eventually erupted 13 hr after the breaking and escaped from the Sun, developing to a fast coronal mass ejection, and P2 stayed. But the mass in P1 falling down to P2 in the eruption suggests that the global magnetic fields over P1 and P2 were still connected to each other prior to the eruption. The reconnection process breaking the filament occurred outside the filament, and P1 and P2 were located almost at the same altitude, so the fashion of the filament partial eruption studied here differs from that of the "double-decker model" and that of reconnection inside the filament. Analyzing the decay indices of the background fields above P1 and P2, n_1 and n_2, showed that the altitude where n_1 exceeds the critical value of $n_c = 1.5$ for the loss of equilibrium or the torus instability is lower than that where $n_2 > n_c$, and that $n_1 > n_2$ always holds at all altitudes. Combining this fact with that the eruption occurred 13 hr after filament was broken by reconnection, we conclude that the eruption of P1 was triggered by the loss of equilibrium or the torus instability in the configuration, and magnetic reconnection breaking the filament helped weaken the confinement of the background field on P1, allowing P1 to erupt. Detailed features of the eruption and the corresponding physical scenario were also discussed.

Key words: Sun: activity – Sun: filaments – prominences – Sun: coronal mass ejections (CMEs) – Sun: flares – Sun: magnetic fields

1. Introduction

Coronal mass ejections (CMEs) and solar flares are the most energetic eruptive phenomena in the solar system and can be hazardous to communications and energy infrastructure on Earth because of the large quantities of magnetized plasma, full wave band electromagnetic radiation, and energetic particles released into the interplanetary space (Forbes et al. 2006; Chen 2011; Schmieder et al. 2015). They have received considerable attention both from observations and theories. CMEs and flares are always believed to be closely associated with filament eruptions (Zhou et al. 2003; Jing et al. 2004; Chen 2011; Schmieder et al. 2013; Cheng et al. 2017; Guo et al. 2017), theories suggest that these three distinct phenomena are different manifestations of a single physical process of energy release by magnetic reconnection (Lin et al. 2003).

However, the pre-eruption configuration of filament is still elusive, which could be sheared arcades with dipped magnetic fields (Mackay et al. 2010; Chen et al. 2020), or a magnetic flux rope (MFR) in which a group of coherent helical field lines twist one or more turns about a common axis (Liu 2020). In most cases, pre-eruption configuration of filament is modeled as an MFR where filament material is located (Low & Hundhausen 1995; Aulanier & Demoulin 1998; Amari et al. 2014; Xia et al. 2014; Guo et al. 2019; Titov et al. 2022). Such a scenario has been observationally confirmed by many authors (e.g., see Zhang et al. 2012; Cheng et al. 2014a; Song et al. 2014; Zhang et al. 2015a; Liu et al. 2016). When an MFR including the filament completely escapes from the Sun, developing to a CME, the corresponding eruption is categorized as a full/successful eruption (Kahler et al. 1986; Zhang & Wang 2001; Wang et al. 2003; Nagashima et al. 2007; Cheng et al. 2013). If the MFR does not escape from the Sun at all or returns to the Sun, the associated filament eruption is defined as confined/failed eruption (Ji et al. 2003; Alexander et al. 2006; Liu et al. 2009; Guo et al. 2010a; Kuridze et al. 2013; Li & Ding 2017; Yan et al. 2020; Zhong et al. 2021; Li et al. 2022b).

In addition to the above two types of eruptions, the third type of the eruption exists in which only part of the filament is expelled from the Sun, and the other part is left (Tang 1986; Pevtsov 2002; Shen et al. 2012; Zhang et al. 2015b; Bi et al. 2015; Chen et al. 2018). This type of eruption is known as the partial eruption. It has been widely accepted that the partial erupting filament often experiences breaking horizontally or vertically. For example, Zuccarello et al. (2009) found that partial eruption was likely to occur when the pre-eruption configuration of a filament was a horizontally broken MFR, i.e., a non-fully coherent MFR (Cheng et al. 2018). In comparison, the vertical filament breaking invoking partial eruptions has been more frequently observed. Gilbert et al. (2000) found that a majority of the eruptive prominences vertically split into escaping and remaining material after examining 54 Hα prominences. Similar splitting was also found by Zhang et al. (2022) in an eruptive prominence. Recently, a filament splitting vertically caused by magnetic reconnection between the filament magnetic field and its ambient loops was reported by Dai et al. (2022) on a partial eruption obtained in 10 830 Å with high-resolution by the 1.6 m New Solar Telescope at the Big Bear Solar Observatory (Cao et al. 2010).

However, whether splitting occurs before or during the eruption is still an open question. Liu et al. (2012) suggested that a partially erupting filament was already vertically split into two parts before the eruption, and only the upper part erupted while the lower one survived the eruption. They proposed a "double-decker filament" model to explain the partial eruption. The model shows that the configuration of the partially erupting filament is composed of a flux rope above a sheared magnetic arcade (Awasthi et al. 2019) or an already vertically split MFR (Chen et al. 2021). Kliem et al. (2014b) later confirmed this idea via a three-dimensional (3D) magnetohydrodynamic (MHD) simulation, and they believed that splitting of the MFR occurred in the pre-eruptive stage. In addition, the idea of "double-decker filament" was also confirmed by observations of Cheng et al. (2014b) and Zheng et al. (2019), who suggested that a complete MFR splits vertically into a double-decker MFR system prior to the eruption. More recently, Pan et al. (2021) also revealed the pre-eruption splitting of a single filament prior to a consequent partial eruption.

Unlike pre-eruption splitting fashion, Gilbert et al. (2001) suggested that an MFR may split in the course of the eruption if the magnetic reconnection takes place within it. This scenario of the partial eruption was demonstrated by the partially expelled-flux-rope (PEFR) model of Gibson & Fan (2006a) through a 3D MHD numerical simulation, in which an MFR was broken into an upper rope and a lower one by internal reconnection during the eruption, in which the upper rope escapes and the lower one survives. Such a partially ejected MFR model for partial filament eruption was further explored in detail by Gibson & Fan (2006b) and Gibson & Fan (2008). It is worth mentioning that an ideal MHD simulation implemented by Birn et al. (2006) showed that a kink-unstable MFR may also break into an escaping piece and a remaining piece in the eruption when the MFR possesses high twist of at least 4.5 turns. Liu et al. (2008) found some observational evidences for the internal reconnection-induced MFR splitting during eruption for the first time, supporting the partial eruption scenario of Gibson & Fan (2006a). Then, Tripathi et al. (2009) and Tripathi et al. (2013) also noticed that a filament-hosting MFR was vertically split into two parts in the eruption by internal magnetic reconnection. Later, Cheng et al. (2018) dug out more unambiguous evidences for vertical splitting of the MFR during the partial eruption. On the other hand, splitting of the filament caused by magnetic reconnection outside the filament prior to the eruption was seldom reported. An example of the filament eruption invoked by magnetic reconnection outside the filament was given by Li et al. (2022a). They noticed that reconnection took place between the field of a new emerging magnetic structure and that associated with part of an existing filament, creating a new piece of filament with a footpoint anchored to the region where the new magnetic field emerged. Eventually, the new piece of the filament erupted.

In the present work, we report a case in which a large-scale filament was broken into two pieces, one piece eventually erupted, and another piece remained still. Obviously, our case is different from that of Li et al. (2022a) such that no new filament was created, and what erupted is a piece of the pre-existing filament. This provides us an opportunity to look into details of a different type of breaking of the filament and the consequent partial filament eruption. Section 2 describes the instruments and observational data involved in this work. Section 3 displays our results. Discussions and interpretations are given in Section 4. Finally, in Section 5, we summarize this work.

2. Instruments and Data

The data used in this work include those in Extreme Ultraviolet (EUV) and Hα, the magnetogram, as well as the photospheric continuum intensity images. The EUV data were obtained by the Atmospheric Imaging Assembly (AIA) on board Solar Dynamics Observatory (SDO; Pesnell et al. 2012), covering the full disk of the Sun in seven EUV, three Ultraviolet (UV) and white-light channels with time cadence of 12 s and the pixel size of $0\farcs6$ (Lemen et al. 2012). The magnetograms were obtained by the Helioseismic and Magnetic Imager (HMI; Scherrer et al. 2012; Schou et al. 2012) on board SDO, which provides vector magnetograms, line of sight (LOS) magnetograms and photospheric continuum intensity images of the full solar disk with a pixel size of $0\farcs5$ in Fe I 6173 Å (Hoeksema et al. 2014). In this work, we use the LOS

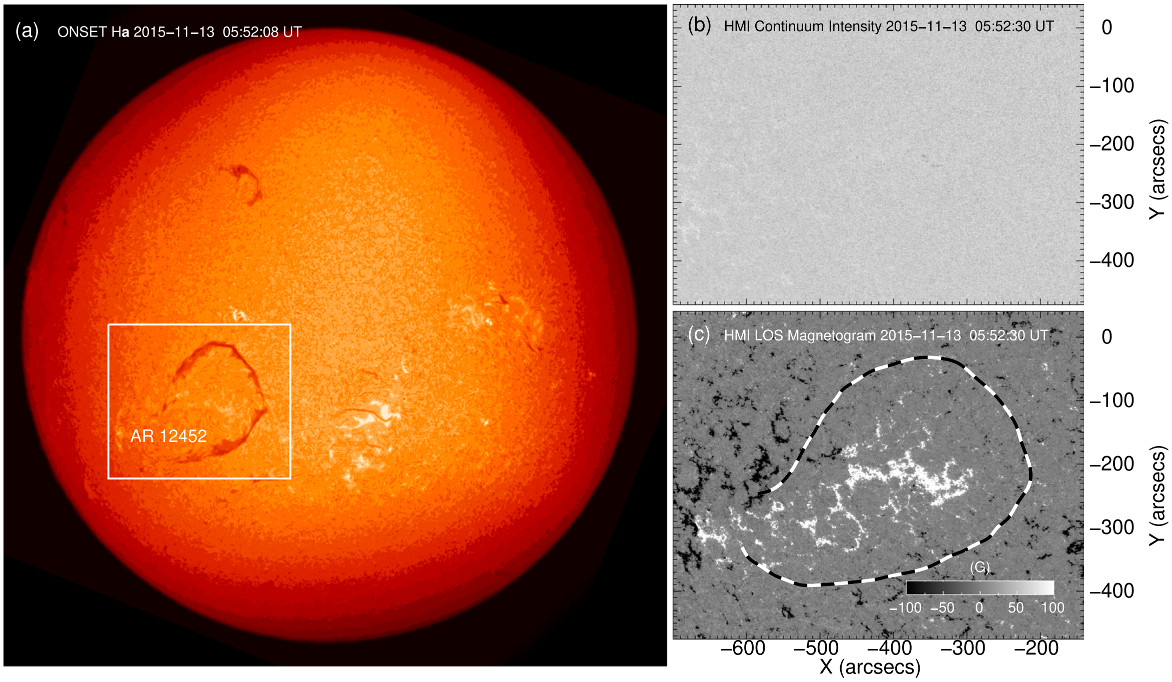

Figure 1. Multi-wavelength overviews of the filament. (a) The full disk of the Sun in Hα of ONSET, the white rectangular box denotes the FOV of panels (b) and (c). (b) The normalized HMI continuum intensity image. (c) The LOS magnetogram of HMI at the photosphere, and the black and white curve represents the filament shown in panel (a).

magnetograms with time cadence of 45 s to calculate the magnetic flux, and those with time cadence of 720 s to extrapolate the background magnetic field. The signal-to-noise ratio of the latter is high compared to that of the former.

The Hα data were obtained by the Optical and Near infrared Solar Eruption Tracer (ONSET; Fang et al. 2013), which is a multiwavelength telescope, and observes the Sun in Hα, He I 10 830 Å, as well as white-light in 3600 Å and 4250 Å in a partial-disk observation mode with high spatial resolution (1″ or better) and high time cadence (better than 1 s), or a full-disk observation mode with time cadence of 1 minute. The Hα data in both partial- and full-disk modes are used here. In addition, the Hα data from the Global Oscillation Network Group (GONG; Harvey et al. 1996) are also employed to investigate the filament eruption process that was beyond the time interval of the ONSET observation.

Moreover, in order to determine whether an eruption is successful or failed, we make use of data from the coronagraph 2 (C2) of the Large Angle and Spectrometric Coronagraph (LASCO; Brueckner et al. 1995) onboard the Solar and Heliospheric Observatory (SOHO; Domingo et al. 1995). In addition, the information on CMEs given by LASCO CME catalog,[6] the soft X-ray (SXR) 1–8 Å flux data from the Geostationary Operational Environmental Satellite (GOES) are also used in the present work.

3. Results

Figure 1 displays images of the large-scale filament of interest observed in different wavelengths by various instruments on ground and in space on 2015 November 13. The main body of the filament seen in Hα shows a horse-shoe-like shape with a length of $\sim 8.5 \times 10^5$ km (Figure 1(a)), and its structural features in the quasi-static evolution stage have been studied by Kang et al. (2023) in detail. The normalized HMI continuum intensity in Figure 1(b) shows that no large sunspot existed in active region (AR) 12452 where the filament was located. Meanwhile, the magnetic field of the region is weak and diffuse (See Figure 1(c)). These two features indicate that the area is a decaying, diffuse and weak AR.

On 2015 November 7, the filament entered the field of view (FOV) of AIA for the first time, then experienced a pre-eruption splitting process, and erupted partially at about 21:15 UT On November 15. By using the method of Guo et al. (2010b) and Chen et al. (2014), we found that the filament had an MFR configuration (Kang et al. 2023). Since the complex geometrical structure and weak background magnetic field, the magnetic structure of the filament cannot be constructed by using the traditional nonlinear force-free field (NLFFF) extrapolation approach (Wiegelmann 2004). Instead, we used

[6] https://cdaw.gsfc.nasa.gov/CME_list/

the MFR embedding method developed by Titov et al. (2018) to construct the magnetic configuration of the filament in 3D successfully (Kang et al. 2023). In the present work, we are looking into the details of splitting, and tracking the consequent eruption of the filament.

3.1. Filament Splitting or Breaking

Analyzing the behavior of the filament seen in different wavelengths indicates that the overall structure of the filament is stable although some local changes could be noticed. A set of Hα images at different times are displayed in Figures 2(a1) through 2(a4), their counterparts in 304 Å and 171 Å are displayed in Figures 2(b1) through 2(b4) and in Figures 2(c1) through 2(c4), respectively, and Figures 2(d1) through 2(d4) display the corresponding magnetograms. Comparing the filament in Hα at 05:00 UT (Figure 2(a1)) on 2015 November 12 with that at 09:00 UT on 2015 November 13 (Figure 2(a2)), we found that the change in the shape of the Hα filament could be recognized, and the overall shape of the filament channel in 304 Å and 171 Å (Figures 2(b2)–(c2)) showed no apparent change. But a small new magnetic structure did appear at the right upper corner of the image (See Figures 2(a2) through 2(d2)). This small structure belongs to AR 12453 that emerged before 09:00 UT on 2015 November 13, and a set of associated magnetic loops L1 could be seen (Figures 2(b2)–(c2)) in the course of emerging, AR 12453 slowly approached to the filament (comparing panels in Figures 2(a2)–(d2) with that in Figures 2(a3)–(d3) and (a4)–(d4)).

By 04:32 UT on 2015 November 14, AR 12453 got close to the filament seen in Hα (Figure 2(a3)), and a set of newly formed magnetic structure N1 connecting the main axis of the filament to AR 12453 (Figures 2(b3)–(c3)). At 08:31 UT on 2015 November 15, the filament in Hα (Figure 2(d1)) split at the location near AR 12453. Meanwhile, another set of magnetic structure N2 appeared, connecting the filament to AR 12453 as well (Figures 2(b4)–(c4)). These features indicate that the topological connectivity of the magnetic field in the filament changed, implying the occurrence of magnetic reconnection between the newly emerging magnetic field in AR 12453 and that around the filament. This causes a pre-eruption splitting of the MFR structure in the filament.

Figure 2(e) reveals that the emergence of AR 12453 started at about 07:30 UT on 2015 November 12 and stopped about 10:00 UT on 2015 November 13, lasting about 27.5 hr. In this period, a small magnetic structure gradually emerged in AR 12453 (See the images surrounded by the white box in Figure 2(d3)), and filament seen in Hα split into two pieces, P1 and P2 (see Figure 2(a4)). In order to examine the emergence location or movement characteristics of the new fluxes during the emergence of AR 12453, we arranged the magnetic flux distribution along line S1S2 in Figure 2(d3) at different moments to obtain the time-variation of the magnetic flux distribution along the line S1S2 in Figure 2(f). We note that between 10:00 UT and 14:00 UT on 2015 November 13, AR 12453 has a tendency to move toward the solar equator with an average velocity of about 0.29 km s^{-1}; however, it is also possible that this is a visual effect caused by the constant appearance of new magnetic structures at different positions. In either case, this led to magnetic reconnection between the magnetic field around the filament and the newly emerging magnetic field, eventually causing the pre-eruption splitting of the large-scale horse-shoe-like filament.

3.2. Partial Eruption of the Filament

After the pre-eruption splitting, part of the large-scale horse-shoe-like filament, P1, erupted at about 21:15 UT on 2015 November 15. Figures 3(a1)–(a3) show the Hα images at three different moments during the eruption, while Figures 3(b1)–(b3), 3(c1)–3(c3) and 3(d1)–3(d3) show the AIA 193 Å, 304 Å and LASCO/C2 images at the corresponding moments, respectively. It can be seen that the eruption of this filament also triggered the eruption of another nearby filament (the filament F2 marked in Figures 3(a1)–(a2)) (interested readers refer to Hou et al. 2020 for a detailed study of this eruption). By comparing the SOHO/LASCO C2 observations, we can also determine whether the eruption of this filament successfully developed to a CME. Within the time interval of several hours before and after the eruption of P1, three partial halo CMEs were observed by LASCO/C2 (Figures 3(d1)–(d3)). The first one was very slow and might not be a regular one in the normal sense although it was identified with a CME by the SOHO/LASCO catalog, but the third one was indeed following the eruption of the filament F2 (see also Hou et al. 2020).

Hα observations indicate that after the eruption of P1, P2 still remained in the source region (Figure 3(a3)), and existed for about 10 hr (13:39 UT on 2015 November 16) after the eruption (Figure 3(a4)). We also noticed that some mass in P1 fell down to P2 in the eruption, which indicates that the filament eruption belongs to a partial eruption, and the global magnetic fields over P1 and P2 prior to the eruption were connected to each other. In addition, we also notice that in the original location of P1, a filament channel connected to the newly emerging AR 12453 (Figure 3(a4)), which can be identified by a set of well aligned Hα fibrils (Zirker et al. 1997). We marked the region of aligned Hα fibrils with two black dashed lines, which outlines the filament channel associated with P1. Both of them existed for a relatively long time, and are transequatorial (Figure 3(a4)), and could be recognized in AIA 304 Å image as well (Figure 3(c4)).

The eruption of the horse-shoe-like filament consisted of three stages. Watching the Hα and AIA 304 Å movies carefully, we realize that apparent mass motion inside the south end of the horse-shoe-like filament could be seen at about

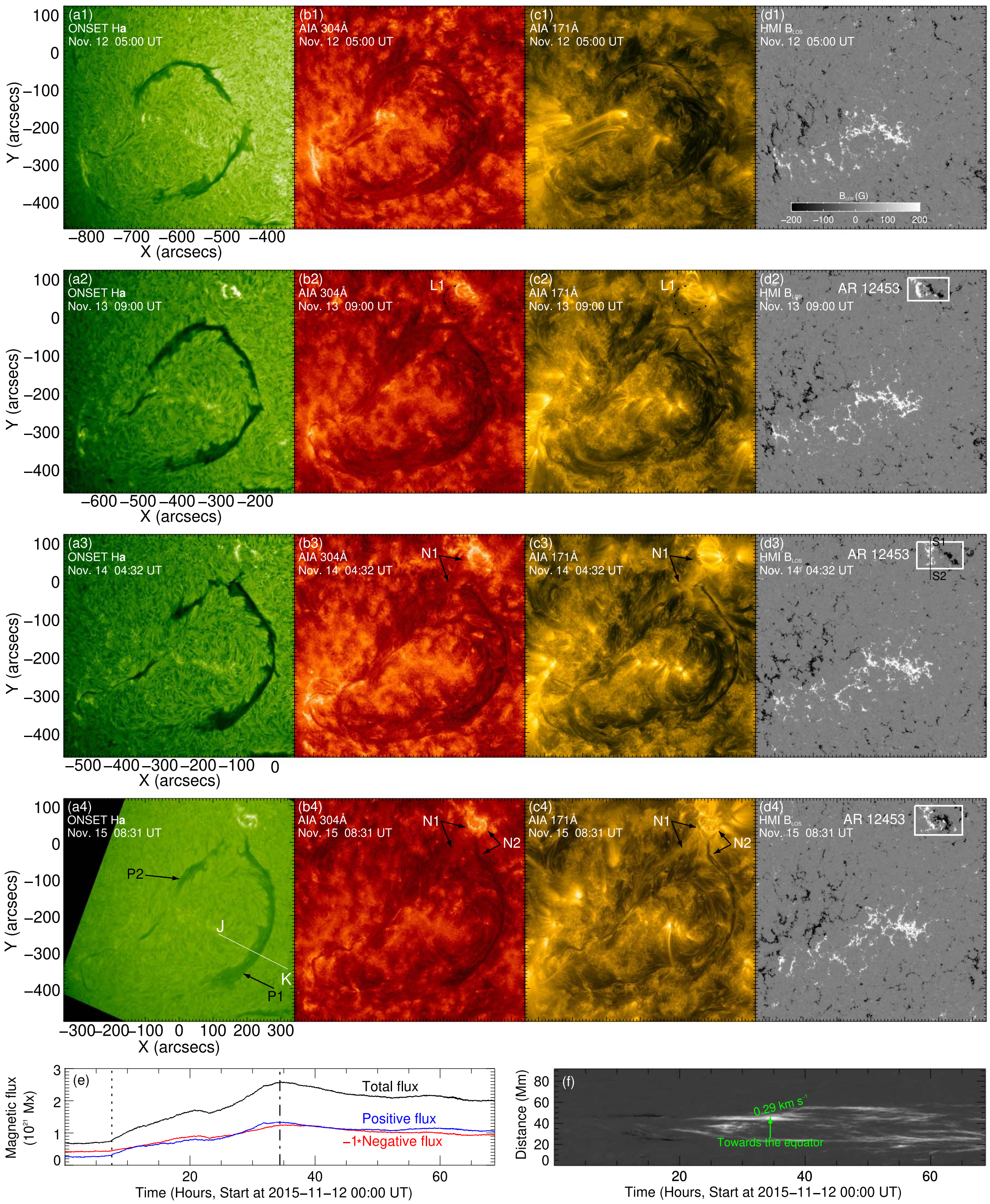

Figure 2. (a1)–(a4) Time sequence of ONSET Hα images displaying the pre-eruption splitting of the filament. The white line JK in panel (a4) represents the location where time-distance diagrams in Figure 4 will be done. (b1)–(b4) Counterparts of panels (a1)–(a4) in AIA 304 Å. (c1)–(c4) Counterparts of panels (a1)–(a4) in AIA 171 Å. (d1)–(d4) Time sequence of HMI LOS magnetograms displaying the emergence of AR 12453. The black dotted lines in panels (b2) and (c2) represent a set of newly emerging magnetic structure from AR 12453 shown in panel (d2). (e) Variations of total (black), positive (blue), and absolute negative (red) magnetic flux in AR 12453 vs. the time. (f) The distance-time diagram along the black line S1S2 in panel (d3).

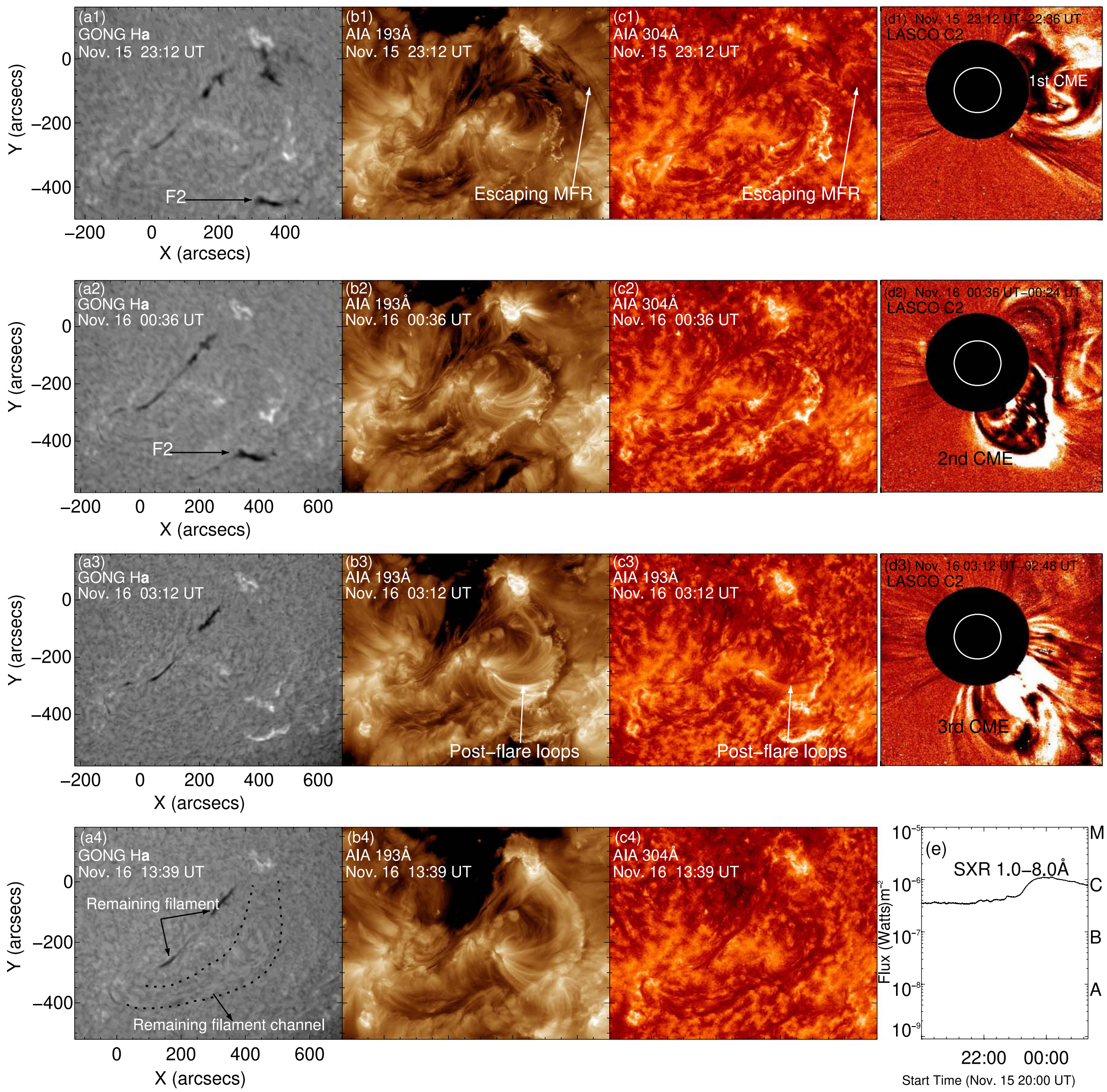

Figure 3. (a1)-(a3) Time sequence of GONG Hα images displaying the partial eruption of the filament. (b1)–(b3) Counterparts of panels (a1)–(a3) in AIA 193 Å. (c1)–(c3) Counterparts of panels (a1)–(a3) in AIA 304 Å. (d1)–(d3) LASCO C2 white-light running-difference images showing the partial eruption is successful. (a4)–(c4) The remaining filament and filament channel in Hα, 193 Å and 304 Å about 10 hr after the eruption. (e) GOES SXR 1.0–8.0 Å flux showing the flare associated with filament eruption. An animation of GONG Hα, 304 Å images and LASCO C2 white-light running-difference images is available. The animation starts at 15:00 UT on 2015 November 15 and ends at 07:00 UT on 2015 November 16. The duration of the video is 38 s.

13:25:14 UT, followed by the slow expansion of the southwest section of the filament seen in AIA 304 Å starting at about 15:12:06 UT. This was the first stage of the eruption. Three hours later, the front of a faint and very slow CME at speed of 86 km s^{-1} appeared in the FOV of LASCO C2 seen in the 18:00:06 UT-17:48:05 UT running difference movie. We note here that it is the CME online-catalog (https://cdaw.gsfc.nasa.gov/CME_list/) that defined it a CME, but it is too faint and too slow to determine whether it was a separated event independent of expansion of the filament. We shall discuss this issue shortly.

P1 started to expand westward apparently at about 21:00 UT, which could be recognized in Hα, AIA 304 Å, and AIA 193 Å movies, and then quickly developed to a CME appearing in the FOV of LASCO/C2 at 22:00:00 UT. This is the take-off stage of the P1 eruption. The second eruption started at 22:24:06 UT with more violently thrusting of the northeast section of P1 outward, and the consequent CME was seen in the LASCO/C2 FOV at 23:12:11 UT, associated with a two-ribbon flare occurring on the solar surface that could be recognized in AIA 304 Å and AIA 193 Å images. Meanwhile, a group of flare loops were seen in AIA 193 Å to anchor at flare ribbons with their two ends. The data of soft X-ray flux showed that a flare of class C1.2 took place at 23:20 UT on 2015 November 15 (Figure 3(e)).

This event began with a sequence of eruptions of filaments, CMEs, and eventually a two-ribbon flare. A very small brightening area prior to the filament eruption was observed in both Hα and AIA images north to the filament (see Figures 2(a2) through 2(a4), 2(b2) through 2(b4), and 2(c2) through 2(c4)), which suggests that magnetic reconnection that causes the filament to break was slow and confined, and did not show apparent energetic feature. Therefore, the event could be considered fitting to the scenario that magnetic reconnection helps weaken the confinement of the background field overlying the filament, and allows the catastrophic loss of equilibrium to occur, leading to the eruption eventually. We conclude that triggering the eruption could be purely ideal MHD, and magnetic reconnection is not a necessity, but the consequent evolution in the disrupting configuration definitely needs reconnection to diffuse the magnetic field fast enough, otherwise the catastrophe cannot develop to a plausible eruption (e.g., see also detailed discussions of Lin & Forbes 2000; Lin 2002 and Lin & van Ballegooijen 2002).

This three-stage eruption started with the slow expansion of a small part of the long horse-shoe-like filament. The evolutionary behavior of this process seems to fit the way of non-catastrophe eruption described by Lin & van Ballegooijen (2002). Impacted by this gradual eruption, the other parts of filament and the associated magnetic configuration quickly loses their equilibrium in the catastrophic fashion, resulting in the second CME at speed of more than 500 km s^{-1}. It is the second eruption that led a smaller filament (F2) to the south of the large filament to erupting more violently, which means that the background magnetic field around F2 was destroyed. The confinement of F2 was thus lifted, and the magnetic structure around F2, as well as the associated plasma, eventually thrusted outward rapidly, giving rise to the third CME, which has been investigated by Hou et al. (2020) in detail, so we will not discuss much of the third eruption in the present work.

3.3. Kinematic Features of the Eruptive Filament

To look into the kinematic behavior of the eruptive filament, we create a time-sequence of the brightness distribution along white line JK in Figure 2(a4), and Figures 4(a) through 4(e) display such time-sequences of brightness distributions in AIA 171 Å, 193 Å, 211 Å, 304 Å, and GONG Hα, respectively. We notice that the section of the filament around line JK started to gradually move upward at about 05:00 UT with speed of 0.38 and 0.34 km s^{-1} in AIA and Hα, respectively. This process lasted about 13 hr and could not be identified in images easily. This is consistent with the characteristics of the first stage of the filament activity, which was too weak to be recognized. According to the evolutionary behavior of the filament prior to the eruption described by the catastrophe model of the solar eruption (e.g., see Lin et al. 2003), this process is the quasi-static one in which the magnetic configuration is in the equilibrium before it reaches the critical state. At around 18:00:04 UT, the SOHO/LASCO CME catalog identified a very gradual CME appearing in the FOV of LASCO/C2, and the corresponding height-time data given in the catalog leads to a speed of 86 km s^{-1} for the CME (see Figure 4(f)). But as mentioned earlier, whether it is a CME of the usual sense is questionable. We note here that, on the other hand, manifestations of the filament in this stage constituted the precursor of the subsequent filament eruption.

In the second stage of the eruption, the apparent velocity of the filament seen in AIA 171 Å, 193 Å, 211 Å is about 10.5 km s^{-1}, and those in AIA 304 Å and GONG Hα are 12.5 km s^{-1} and 9.7 km s^{-1}, respectively. Difference in velocities seen in various wavelengths results from both errors in data processing and the fact that different parts of the filament may move at different velocities. The consequent CME seen in the LASCO/C2 FOV propagated at speed of 508 km s^{-1} on average according to the data in the SOHO/LASCO CME Catalog at http://cdaw.gsfc.nasa.gov/CME_list/ (see also Figure 4(g)).

Meanwhile, two bright flare ribbons seen in AIA images/movie appeared on the solar surface, and separated from each other at speed of about 24.2 km s^{-1} at the very beginning, then quickly dropped to about 6.9 km s^{-1} in 15 minutes. Relatively, the two flare ribbons seen in Hα image were not as bright as in AIA images, which implies that magnetic reconnection driving the eruption was not energetic enough, and the energy released could just heat the low corona and the high chromosphere only. In addition, sudden decrease and/or vanishing in the speed of the ribbon separation indicates that the disrupting magnetic structure was located within a relatively confined area beyond which the magnetic structure possesses different topology (e.g., see also discussions of Lin 2004b). This confirms the conclusion of Kang et al. (2023) such that three magnetic structures of different topologies existed around the large horse-shoe-like filament.

Behaviors of the above two CMEs seen in LASCO/C2 suggest that they were different processes in origin. Following splitting of the large filament, the magnetic field passing around the filament expanded very slowly as a result of the evolution in the global configuration, leading to the first very slow CME. On the other hand, the evolutionary feature of P1 within a time interval more than 13 hr as shown in Figures 4(a) through 4(e) before erupting is typically quasi-static, and the eruption of P1 should be eventually triggered by the catastrophic loss of

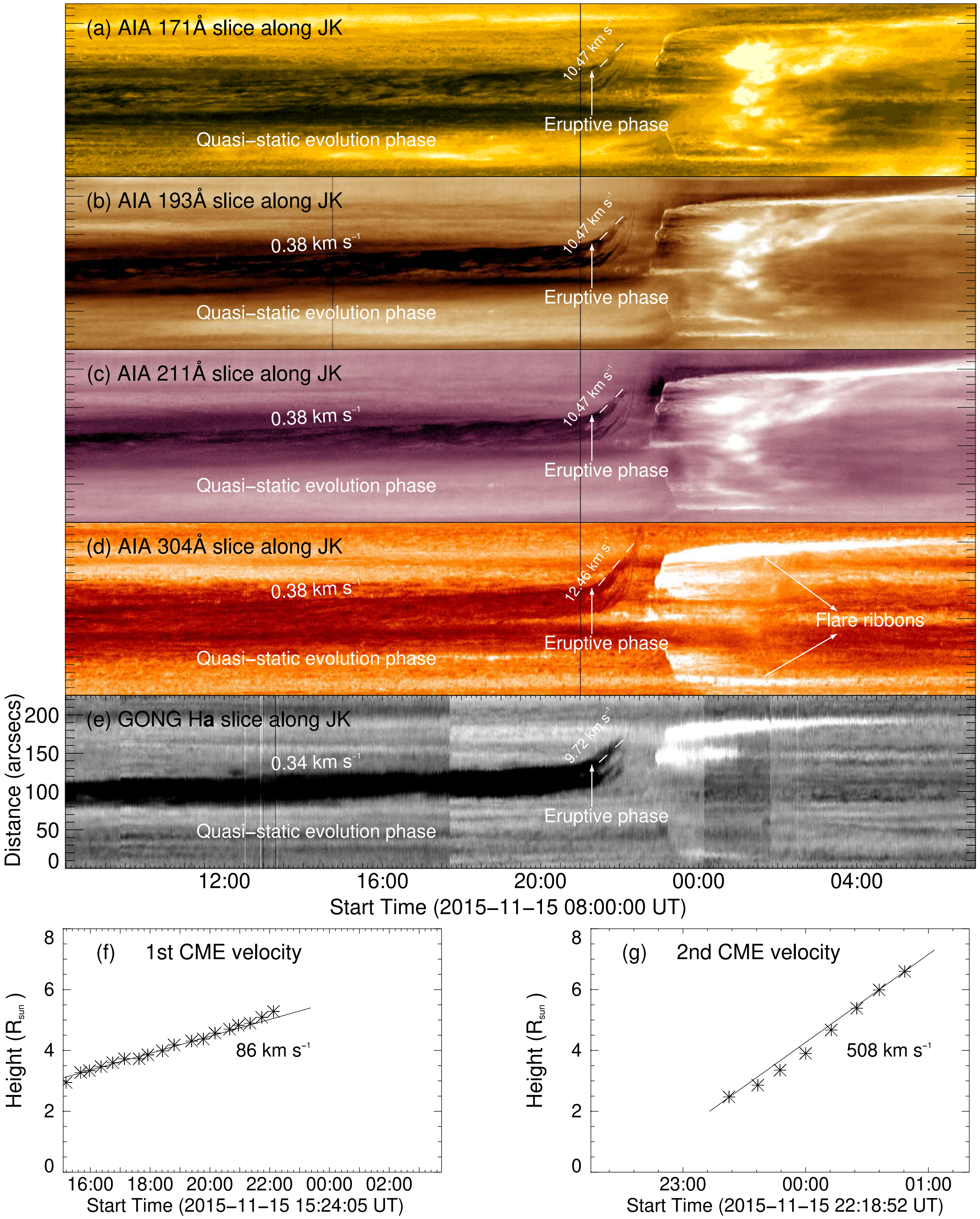

Figure 4. (a)–(e) The distance-time plots of the AIA 171 Å, 193 Å, 211 Å, 304 Å and GONG Hα images along the slice JK shown in Figure 3(a1). (f) The height-time measurements of the first CME (asterisks) in the FOV of LASCO C2 and the corresponding linear fit (the black line). (g) The height-time measurements of the second CME (asterisks) in the FOV of LASCO C2 and the corresponding linear fit (the black line).

equilibrium in the magnetic structure, creating a CME with speed of 508 $km\ s^{-1}$ (see also Figure 4(g)), which can be considered fast according to Pant et al. (2021). As we pointed out earlier, this eruption was triggered by the catastrophic loss of equilibrium in the magnetic configuration, and the fact that it created a C1.2 flare occurring about 2 hr after the take-off of the filament and a CME propagating at speed of 508 $km\ s^{-1}$ implies that the strength of the background magnetic field might be around 30 G according to Lin (2002) and Lin (2004a).

3.4. Catastrophic Loss of Equilibrium in the Magnetic Configuration Including the Filament

With the impact of the new emerging flux occurring northwest to the horse-shoe-like filament, the filament split into west (P1 in Figure 5(a)) and east (P2 in Figure 5(a)) parts, the west part eventually erupted, and the east one left. Behaviors and P1 shown in Figures 4(a) through 4(e) and in the associated movies indicate that P1 experienced a very slow and long evolutionary phase, in which the global structures remained almost no change, and the altitude displayed a fairly gradual increase at a speed less than 0.5 $km\ s^{-1}$. This phase lasted more than 13 hr before a faster upward motion with speed about 10 $km\ s^{-1}$ was observed at the south part of P1 after 21:00 UT. Therefore, this is a quasi-static evolution stage of P1. In the following time interval of about two hours, the south and the north parts of P1 were successively thrusted out of FOVs of Hα and AIA images, and two CMEs with speeds of 86 $km\ s^{-1}$ and 508 $km\ s^{-1}$, respectively, were subsequently observed by LASCO/C2 as well. Due to the projection effect, the true speeds of filament and CME should be higher than the above values. The above feature of P1 fits the scenario of the catastrophe that triggers the loss of equilibrium in the magnetic configuration (e.g., see also discussions of Lin & Forbes 2000; Lin 2002; Zhang et al. 2012; Cheng et al. 2020). But P2 and the surrounding magnetic structure almost remained unchanged in this process. Different behaviors of P1 and P2 seem to imply different rate of which the background fields around P1 and P2 decay.

The rate of decay in a magnetic field versus the altitude is defined by $n = -d\ln B_0/d\ln h$, where B_0 is the strength of the background magnetic field and h is the altitude from the surface of the Sun (see also Bateman 1978 and Kliem & Török 2006). Apparently, the larger the value of n is, the faster the background field, B_0, decays. To evaluate n in the region of interest, we need to obtain the distribution of B_0 in space. Generally, we are able to get the distribution of B_0 from the results of our previous work (Kang et al. 2023), and alternatively, the distribution of B_0 could also deduced via the approach of the potential field extrapolation (e.g., see also Alissandrakis 1981 and Gary 1989). In principle, both approaches should give the same result at large h since the non-potential feature of the background field dies down faster than the potential one. So, for simplicity, we are using the package of extrapolation procedures included in the Solar Software (SSW) to deduce B_0 distribution in space on the basis of the longitudinal component of the magnetic field on the photosphere surface obtained by SDO/HMI.

Figure 5(a) displays the global feature of the background field in the region of interest at 21:00 UT on 2015 November 15 right before the eruption. The global background field is reconstructed by the package of extrapolation procedures in SSW. The region shown in Figure 5(a) covers the decaying AR 12452 and the new emerging AR 12453 of small scale. We also notice that the horse-shoe-like filament is well confined in the background field. Based on this result, we are able to look into the distribution of the decay index in space.

Figures 5(b1) through 5(b3) display contours of $n = 1.5$ at altitudes of 6.5×10^4 km, 8.5×10^4 km, and 9.5×10^4 km, respectively. Kliem & Török (2006), Zuccarello et al. (2014) and Zhou et al. (2017) believed that 1.5 is the critical value of n at which the torus instability takes place. Forbes & Isenberg (1991) pointed out that the catastrophic loss of equilibrium in the magnetic configuration occurs only if the photospheric background field falls off with height faster than $1/h$. Kliem et al. (2014a) confirmed that the catastrophe and the torus instability in the magnetic configuration are equivalent to each other in triggering the eruption. Figure 5(b1) indicates locations where $n = 1.5$ exist just in several small confined regions, which suggests that the eruption of the filament is not easy if the filament is located at the corresponding height. At higher altitudes, on the other hand, the area outlined by contour $n = 1.5$ becomes bigger and bigger (see Figures 5(b2) and 5(b3)), and eruption could occur relatively easily at these locations.

Furthermore, as we noted earlier, the eruption of the west part of the long filament, namely P1, started from the middle part, and then the other part of P1 successively took off from south to north developing to a fast CME eventually. We also need to address here that the plasma inside the erupting filament was observed to flow down to the south endpoint of P1 as well, which suggests that the eruption did not thrust the whole magnetic structure of the filament, including the plasma inside, outward to interplanetary space, and the connection of magnetic field in the disrupting configuration to the photosphere at the endpoint of P1 still exists in the eruption instead. This indicates that the force acting on the filament is not uniform at different parts of the filament, which results either from that the net force pushing the middle part of the filament is stronger than that pushing the other part, or from that the decay rate of the background magnetic field around the middle part is bigger than that in the other region. It is fairly hard, if not impossible, to test the first case, but not difficult to check whether the second case is true.

Variations of the value of n on average around P1 and P2 versus the height were calculated, and were displayed in

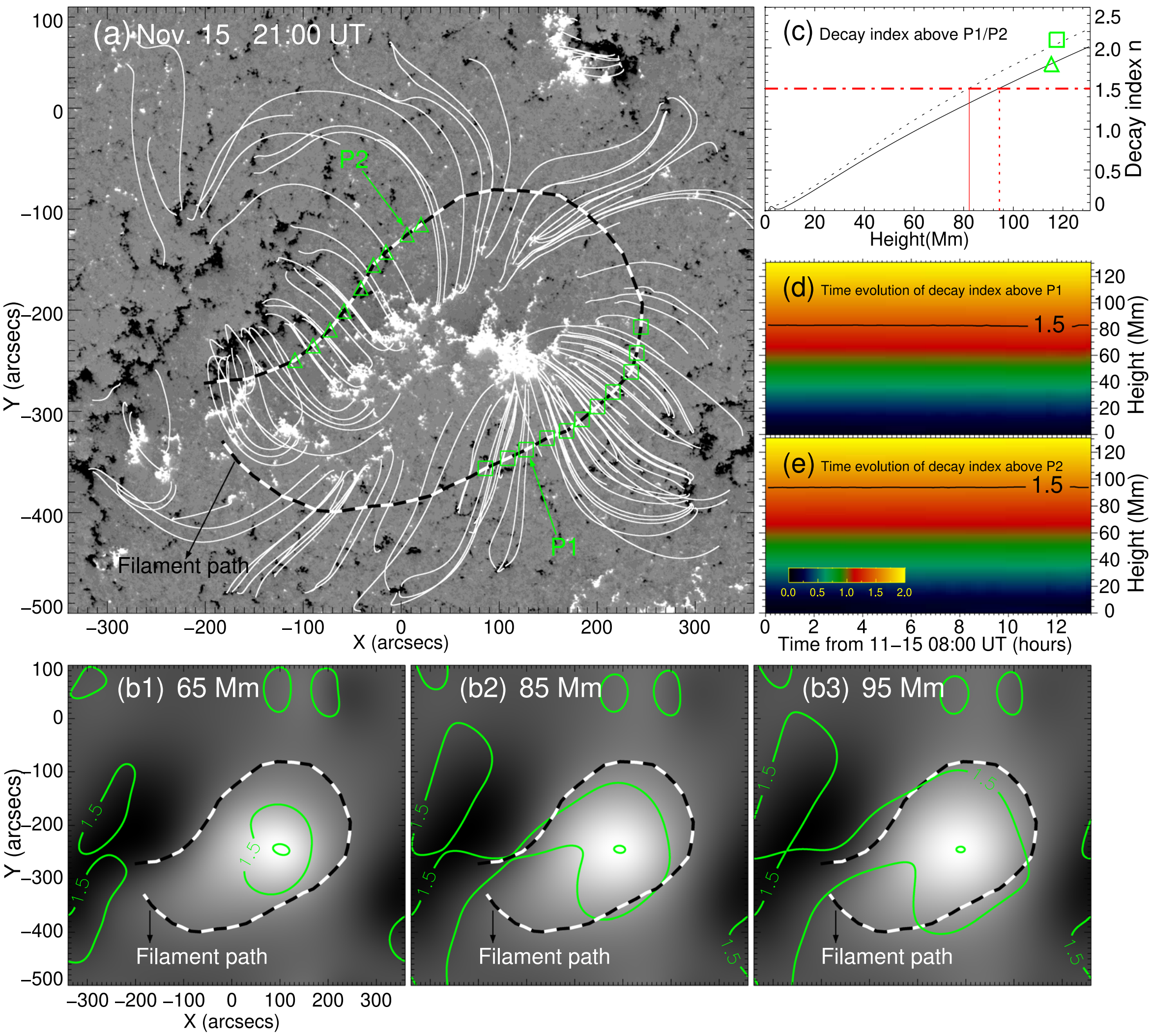

Figure 5. (a) The field lines (white lines) of the extrapolated potential magnetic fields and the filament path (the black and white curve). The green squares and triangles mark two different sections of the filament path, P1 and P2. (b1)–(b3) The contours (green) of decay index with value of 1.5 at various height overlaid with corresponding LOS magnetogram (grayscale image) and filament path (the black and white curve). (c) Variations of average decay index of P1 (the black dotted line) and P2 (the black solid line) vs. height. The red horizontal dotted–dashed line marks the critical decay index of the torus instability. The red vertical solid and dotted lines mark the critical heights of the torus instability above P1 and P2, respectively. (d) Variations of average decay index above P1 vs. time. (e) Variations of average decay index above P2 vs. time.

Figure 5(c). The dashed curve is for P1 and the solid one for P2. We noticed that the decay rate of the background field around P1 is always bigger than that around P2, which implies that the confinement of the background field on P2 is stronger than that on P1. This can also be seen from the locations on the two curves where the n reaches the critical value of 1.5 such that the value of n for P1 reaches 1.5 at altitude of 8.2×10^4 km, and that for P2 reaches the same value at 9.4×10^4 km. Therefore, we are sure that, at least, the background field above P1 decays faster than that above P2 so that P1 eventually erupted completely, and the basic structure of P2 remained almost unchanged.

In addition, we looked into the evolution in the above two curves and the results are given in Figures 5(d) and (e), respectively. Minor fluctuations of average values of n at different times could be noticed, but the locations where $n = 1.5$ remained nearly unchanged. This means that the fashion in which the background field around the filament decays is almost time-independent. Thus, we attain such a scenario that variations of the background field drive the filament upward, P1 entered the region in which $n \geqslant 1.5$ easily, and then quickly erupted as a result of the torus instability, which could explain the behavior of the filament observed.

4. Discussions

As a follow-up of our previous work (e.g., see Kang et al. 2023), we investigated in detail the evolutionary behavior of a long horse-shoe-like filament that had existed for about 8 days and 20 hr since it appeared on the solar disk at 00:02 UT on 2015 November 7 for the first time. In most of the time, the filament stayed quasi-statically until a small AR 12453 emerged northwest to the filament on 2015 November 15. AR 12453 started appearing in both Hα and AIA images as two bright ribbons on the solar disk at about 07:00 UT on November 12, associated with a southward expansion/movement of the new magnetic structure as shown in Figure 2(f). Bright arcades connecting the two ribbons could be seen in AIA images but not in Hα images (comparing Figures 2(a2), (b2), and (c2)). Magnetic reconnection between the new magnetic field and the pre-existing magnetic field around the filament took place in the process of flux emerging.

The consequence of the reconnection process is apparent in Hα such that the filament was broken into two sections, P1 and P2, before 08:31 UT on 2015 November 15, and a small stem extended from north end of P1 toward the region where the new flux emerged. Then, P1 gradually disappeared and did not show further significant activities in the following evolutionary stage, and the global configuration of the filament channel seen in AIA images roughly remained unchanged until the eruption. Cartoons in Figure 6 demonstrates the process of the filament breaking.

So it is clear that the eruption took place after breaking of the filament in the present case as reported previously by some authors (e.g., see also Liu et al. 2012; Cheng et al. 2014b; Zheng et al. 2019; Pan et al. 2021, and Chen et al. 2021) although some filaments were also observed to break during the eruption (e.g., see also Liu et al. 2008; Tripathi et al. 2009, 2013, and Cheng et al. 2018). The case reported by Li et al. (2022a) does not belong to either of these two categories. In their case, a new piece of filament was first created by magnetic reconnection between the field in a new emerging magnetic structure and that associated with part of the pre-existing filament. Then the newly formed piece of filament erupted, but the other part of the filament remained unchanging.

Panels in Figure 2(a) and in Figures 2(b4) and 2(c4) suggest that the magnetic reconnection process mentioned above took place at two locations: One was between the new field in the emerging AR and that around the filament, and another one between the new field and that in the loops overlying the filament. The indirect evidences of reconnection are the small bright Hα ribbons seen in Figures 2(a1) through 2(a4), and small EUV ribbons/loops seen in Figures 2(b1) through 2(b4), and 2(c1) through 2(c4), respectively. Magnetic reconnection could occur between the new field and the field in the loops overlying the filament because the north end of the overlying loops was actually located closer to the emerging AR than the filament. This reconnection process diverted the loops sideways or pushed the loops to the higher altitude, helping the eruption of P1 occur. Since such reconnection process occurred at a fairly low rate, on the other hand, it took a very long period, say 13 hr after the filament broke, for the effect of reconnection to show its role in triggering the eruption.

Unlike the case reported by Cheng et al. (2018) that the filament breaks as a result of magnetic reconnection taking place inside the filament during the eruption, breaking of the filament in the present case occurred before the eruption. Also unlike the double-decker filament of which the two components of the filament are located at different heights (e.g., see Liu et al. 2012), two components of the filament studied here were roughly located at the same height.

For the present case, on the other hand, it is not clear whether the new emerging flux directly triggered the eruption after all the eruption occurred 13 hr after the new flux emerged. Considering the fact that the filament studied here was located in a decaying active region, we conclude that the eruption resulted from continuous decaying of the background field, which leads to decrease in the magnetic tension that prevents the loss of the equilibrium in the global configuration from occurring (refer to theoretical discussions on the topic by Isenberg et al. 1993). But the manifestation of P1 eruption and analyses on the decay index in the area do suggest that magnetic reconnection occurring between the new emerging field and the pre-existing field around the Hα filament indeed helps weaken part of the confinement of background field on the north section of P1.

Behaviors of P1 in the eruptive process indicate that the eruption is more likely to be triggered by the catastrophic loss of equilibrium or the torus instability occurring in the magnetic configuration surrounding the south part of P1 where the take-off of P1 started first. Weakening of the confinement on the north section allows thrusting of the south section to lift the north section subsequently, eventually developing to a typical eruption that begins with the disruption of the filament and then produces a two-ribbon flare and a fast CME (e.g., see also detailed discussions of Lin et al. 2003; Lin 2004a, and Kliem et al. 2014a).

In addition, we noticed that the slow CME moving at speed of 86 $\mathrm{km\,s^{-1}}$ and the following fast CME at speed of 508 $\mathrm{km\,s^{-1}}$ should be two components of a single CME. The evolution of the global magnetic configuration first pushed the outmost magnetic field to expand outward, became a slow CME as it reached the height of the solar wind, and continuous evolution of the configuration finally leads to a major eruption. The LASCO CME catalog identified them as two CMEs because these CMEs were of two different courses. The former was probably originating from the gradual expansion of the overall magnetic field in the region of interest, and the latter is a typical eruptive event due to the loss of the equilibrium in the magnetic configuration. The reason why the former was identified with a CME is because the approach to identifying and tracking an eruption is somehow artificial (Yashiro et al. 2004). So the automatically detecting and identifying approach

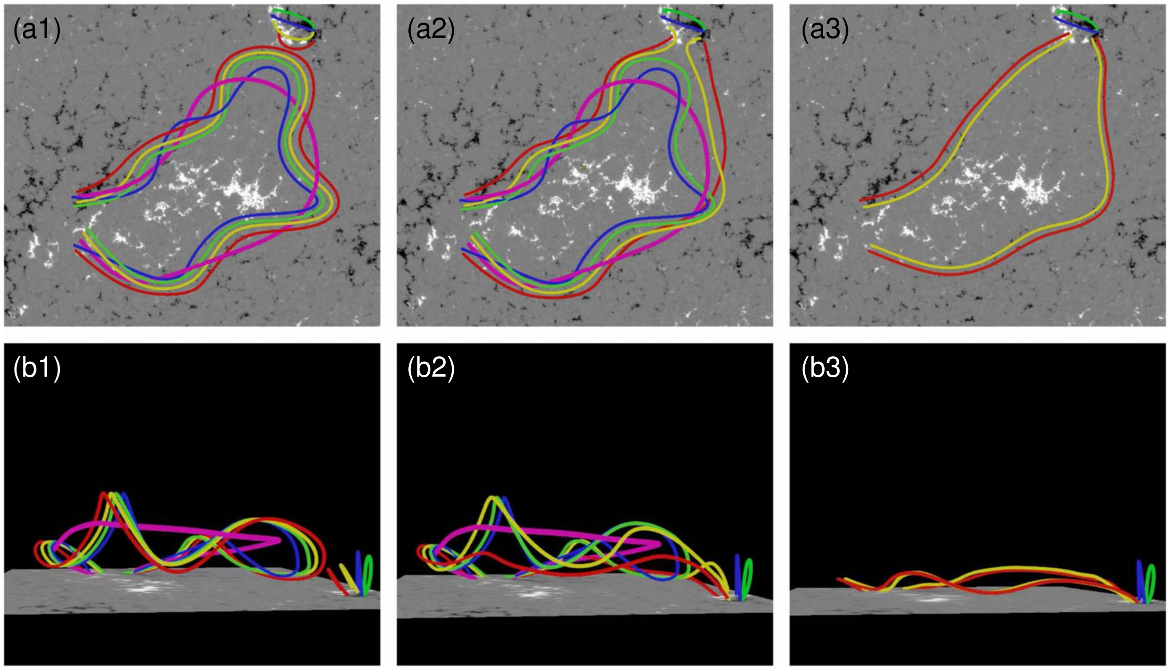

Figure 6. 3D cartoons showing the MFR splitting and the associated partial eruption, overlaid with the LOS magnetogram. Panels (a1)–(a3) display the magnetic topologies seen downward from the top before (a1) and after (a2) the splitting, and after the eruption (a3), respectively. Panels (b1)–(b3) display the same topologies seen from a side view.

developed by Wang et al. (2019) might give more accurate conclusions, and the result could be better if the continuity of the eruptive prominence and the consequent CME in both space and time could be considered simultaneously.

5. Conclusions

Previously, we investigated the magnetic structure of a large horse-shoe-like filament via the regularized Biot–Savart law approach and revealed several interesting and important fine features of the filament (Kang et al. 2023). This filament totally appeared on the solar disk at 05:40 UT on 2015 November 11, and then stayed on the disk quasi-statically for 4 days and 16 hr. Its apparent change occurred after 07:30 UT on November 12 when a small AR 12453 emerged northwest to the filament.

Magnetic reconnection between the new magnetic field and that around the filament destroyed part of the pre-existing magnetic structure, and the large filament seen in Hα completely broke into two sections, P1 and P2, at the north end of the large horse-shoe-like filament after 22:50 UT on November 14. About 13 hr later, P1 gradually disappeared in Hα and commenced to erupt. The eruption started from the middle part of P1, and then brought the other part of P1 to escape from the Sun, developing to a CME at speed of 508 km s^{-1}. Although the filament seen in Hα was broken, the fact that the falling mass from P1 down to P2 during the eruption suggested that the global magnetic field over P1 and P2 still kept connected before the eruption.

We studied the decay index, n, of the background field on average over P1 and P2, and found that n_1 exceeds n_2 at all heights above P1 and P2. This suggests that the confinement of the background field on P1 is weaker than that on P2, so that P1 could erupt and P2 left behind. We thus concluded that it is the reconnection between the new emerging field and the pre-existing field around the large filament that weakened part of the confinement of the background field on the filament, allowing the eruption of P1 to occur. The fact that the eruption took place about 13 hr after the large filament totally broke indicates that reconnection between the new and the old fields did not trigger the eruption directly.

Because the eruption studied here took place after the large filament broke, it is different from the case in which breaking happens inside the filament during the eruption (e.g., see also Cheng et al. 2018). It also differs from that described by the so-called "double-decker" model (e.g., see also Liu et al. 2012) in which two components of the filament are located at different altitudes since the two components of the filament studied here were located at almost the same altitude. Overall, breaking of large filaments, subsequent eruption, as well as the role of magnetic reconnection in the relevant processes are interesting topics, and we shall look into more details in the future.

Acknowledgments

We are very grateful for the referee's valuable comments and suggestions that help improve the paper. This work was supported by the National Key R&D Program of China No. 2022YFF0503804, the Strategic Priority Research Programme of the Chinese Academy of Sciences with grant XDA17040507, the National Natural Science Foundation of China (NSFC) grant 11 933 009, grants associated with the Yunling Scholar Project of Yunnan Province, the Yunnan Province Scientist Workshop of Solar Physics. The numerical computation in this paper was carried out on the computing facilities of the Computational Solar Physics Laboratory of Yunnan Observatories (CosPLYO). The ONSET data are available on courtesy of the ONSET team. The HMI and AIA data used here are available on courtesy of NASA/SDO and the AIA and HMI science teams. The SOHO/LASCO C2 data are available on courtesy of the SOHO and LASCO C2 teams. The GONG and GOES data are available on courtesy of the GONG and GOES teams. We are grateful to the ONSET, SDO/AIA, SDO/HMI, SOHO/LASCO C2, GOES and GONG consortium for the free access to the data. We thank NASA/ADS team for the convenient literature search service very much.

References

Alexander, D., Liu, R., & Gilbert, H. R. 2006, ApJ, 653, 719
Alissandrakis, C. E. 1981, A&A, 100, 197
Amari, T., Canou, A., & Aly, J.-J. 2014, Natur, 514, 465
Aulanier, G., & Demoulin, P. 1998, A&A, 329, 1125
Awasthi, A. K., Liu, R., & Wang, Y. 2019, ApJ, 872, 109
Bateman, G. 1978, MHD Instabilities (Cambridge, MA: MIT)
Bi, Y., Jiang, Y., Yang, J., et al. 2015, ApJ, 805, 48
Birn, J., Forbes, T. G., & Hesse, M. 2006, ApJ, 645, 732
Brueckner, G. E., Howard, R. A., Koomen, M. J., et al. 1995, SoPh, 162, 357
Cao, W., Gorceix, N., Coulter, R., et al. 2010, AN, 331, 636
Chen, H., Duan, Y., Yang, J., Yang, B., & Dai, J. 2018, ApJ, 869, 78
Chen, J., Su, Y., Liu, R., et al. 2021, ApJ, 923, 142
Chen, P. F. 2011, LRSP, 8, 1
Chen, P. F., Harra, L. K., & Fang, C. 2014, ApJ, 784, 50
Chen, P.-F., Xu, A.-A., & Ding, M.-D. 2020, RAA, 20, 166
Cheng, X., Ding, M. D., Guo, Y., et al. 2014a, ApJ, 780, 28
Cheng, X., Ding, M. D., Zhang, J., et al. 2014b, ApJL, 789, L35
Cheng, X., Guo, Y., & Ding, M. 2017, ScChE, 60, 1383
Cheng, X., Kliem, B., & Ding, M. D. 2018, ApJ, 856, 48
Cheng, X., Zhang, J., Ding, M. D., Liu, Y., & Poomvises, W. 2013, ApJ, 763, 43
Cheng, X., Zhang, J., Kliem, B., et al. 2020, ApJ, 894, 85
Dai, J., Li, Z., Wang, Y., et al. 2022, ApJ, 929, 85
Domingo, V., Fleck, B., & Poland, A. I. 1995, SoPh, 162, 1
Fang, C., Chen, P.-F., Li, Z., et al. 2013, RAA, 13, 1509
Forbes, T. G., & Isenberg, P. A. 1991, ApJ, 373, 294
Forbes, T. G., Linker, J. A., Chen, J., et al. 2006, SSRv, 123, 251
Gary, G. A. 1989, ApJS, 69, 323
Gibson, S. E., & Fan, Y. 2006a, JGRA, 111, A12103
Gibson, S. E., & Fan, Y. 2006b, ApJL, 637, L65
Gibson, S. E., & Fan, Y. 2008, JGRA, 113, A09103
Gilbert, H. R., Holzer, T. E., & Burkepile, J. T. 2001, ApJ, 549, 1221
Gilbert, H. R., Holzer, T. E., Burkepile, J. T., & Hundhausen, A. J. 2000, ApJ, 537, 503
Guo, Y., Cheng, X., & Ding, M. 2017, ScChE, 60, 1408
Guo, Y., Ding, M. D., Schmieder, B., et al. 2010a, ApJL, 725, L38
Guo, Y., Schmieder, B., Démoulin, P., et al. 2010b, ApJ, 714, 343
Guo, Y., Xia, C., Keppens, R., Ding, M. D., & Chen, P. F. 2019, ApJL, 870, L21
Harvey, J. W., Hill, F., Hubbard, R. P., et al. 1996, Sci, 272, 1284
Hoeksema, J. T., Liu, Y., Hayashi, K., et al. 2014, SoPh, 289, 3483
Hou, Y. J., Li, T., Song, Z. P., & Zhang, J. 2020, A&A, 640, A101
Isenberg, P. A., Forbes, T. G., & Demoulin, P. 1993, ApJ, 417, 368
Ji, H., Wang, H., Schmahl, E. J., Moon, Y. J., & Jiang, Y. 2003, ApJL, 595, L135
Jing, J., Yurchyshyn, V. B., Yang, G., Xu, Y., & Wang, H. 2004, ApJ, 614, 1054
Kahler, S. W., Cliver, E. W., Cane, H. V., et al. 1986, ApJ, 302, 504
Kang, K., Guo, Y., Roussev, I. I., Keppens, R., & Lin, J. 2023, MNRAS, 518, 388
Kliem, B., Lin, J., Forbes, T. G., Priest, E. R., & Török, T. 2014a, ApJ, 789, 46
Kliem, B., & Török, T. 2006, PhRvL, 96, 255002
Kliem, B., Török, T., Titov, V. S., et al. 2014b, ApJ, 792, 107
Kuridze, D., Mathioudakis, M., Kowalski, A. F., et al. 2013, A&A, 552, A55
Lemen, J. R., Title, A. M., Akin, D. J., et al. 2012, SoPh, 275, 17
Li, L., Peter, H., Chitta, L. P., et al. 2022a, ApJ, 935, 85
Li, L., Song, H., Peter, H., & Chitta, L. P. 2022b, ApJL, 941, L1
Li, Y., & Ding, M. D. 2017, ApJ, 838, 15
Lin, J. 2002, ChJAA, 2, 539
Lin, J. 2004a, SoPh, 219, 169
Lin, J. 2004b, SoPh, 222, 115
Lin, J., & Forbes, T. G. 2000, JGR, 105, 2375
Lin, J., Soon, W., & Baliunas, S. L. 2003, NewAR, 47, 53
Lin, J., & van Ballegooijen, A. A. 2002, ApJ, 576, 485
Liu, R. 2020, RAA, 20, 165
Liu, R., Gilbert, H. R., Alexander, D., & Su, Y. 2008, ApJ, 680, 1508
Liu, R., Kliem, B., Titov, V. S., et al. 2016, ApJ, 818, 148
Liu, R., Kliem, B., Török, T., et al. 2012, ApJ, 756, 59
Liu, Y., Su, J., Xu, Z., et al. 2009, ApJL, 696, L70
Low, B. C., & Hundhausen, J. R. 1995, ApJ, 443, 818
Mackay, D. H., Karpen, J. T., Ballester, J. L., Schmieder, B., & Aulanier, G. 2010, SSRv, 151, 333
Nagashima, K., Isobe, H., Yokoyama, T., et al. 2007, ApJ, 668, 533
Pan, H., Liu, R., Gou, T., et al. 2021, ApJ, 909, 32
Pant, V., Majumdar, S., Patel, R., et al. 2021, FrASS, 8, 73
Pesnell, W. D., Thompson, B. J., & Chamberlin, P. C. 2012, SoPh, 275, 3
Pevtsov, A. A. 2002, SoPh, 207, 111
Scherrer, P. H., Schou, J., Bush, R. I., et al. 2012, SoPh, 275, 207
Schmieder, B., Aulanier, G., & Vršnak, B. 2015, SoPh, 290, 3457
Schmieder, B., Démoulin, P., & Aulanier, G. 2013, AdSpR, 51, 1967
Schou, J., Scherrer, P. H., Bush, R. I., et al. 2012, SoPh, 275, 229
Shen, Y., Liu, Y., & Su, J. 2012, ApJ, 750, 12
Song, H. Q., Zhang, J., Cheng, X., et al. 2014, ApJ, 784, 48
Tang, F. 1986, SoPh, 105, 399
Titov, V. S., Downs, C., Mikić, Z., et al. 2018, ApJL, 852, L21
Titov, V. S., Downs, C., Török, T., & Linker, J. A. 2022, ApJ, 936, 121
Tripathi, D., Gibson, S. E., Qiu, J., et al. 2009, A&A, 498, 295
Tripathi, D., Reeves, K. K., Gibson, S. E., Srivastava, A., & Joshi, N. C. 2013, ApJ, 778, 142
Wang, H., Qiu, J., Jing, J., & Zhang, H. 2003, ApJ, 593, 564
Wang, P., Zhang, Y., Feng, L., et al. 2019, ApJS, 244, 9
Wiegelmann, T. 2004, SoPh, 219, 87
Xia, C., Keppens, R., & Guo, Y. 2014, ApJ, 780, 130
Yan, X., Xue, Z., Cheng, X., et al. 2020, ApJ, 889, 106
Yashiro, S., Gopalswamy, N., Michalek, G., et al. 2004, JGRA, 109, A07105
Zhang, J., Cheng, X., & Ding, M.-D. 2012, NatCo, 3, 747
Zhang, J., & Wang, J. 2001, ApJ, 554, 474
Zhang, J., Yang, S. H., & Li, T. 2015a, A&A, 580, A2
Zhang, Q. M., Ning, Z. J., Guo, Y., et al. 2015b, ApJ, 805, 4
Zhang, Y., Zhang, Q., Dai, J., Li, D., & Ji, H. 2022, SoPh, 297, 138
Zheng, R., Yang, S., Rao, C., et al. 2019, ApJ, 875, 71
Zhong, Z., Guo, Y., & Ding, M. D. 2021, NatCo, 12, 2734
Zhou, G., Wang, J., & Cao, Z. 2003, A&A, 397, 1057
Zhou, G. P., Zhang, J., Wang, J. X., & Wheatland, M. S. 2017, ApJL, 851, L1
Zirker, J. B., Martin, S. F., Harvey, K., & Gaizauskas, V. 1997, SoPh, 175, 27
Zuccarello, F., Romano, P., Farnik, F., et al. 2009, A&A, 493, 629
Zuccarello, F. P., Seaton, D. B., Mierla, M., et al. 2014, ApJ, 785, 88